RESEARCH ARTICLE

Check for updates

Photochemical CO_2 conversion on pristine and Mg-doped gallium nitride (GaN): a comprehensive DFT study based on a cluster model approach†

Valeria Butera [iD] *[a] and Hermann Detz[ab]

The photochemical reduction of carbon dioxide (CO_2) into methanol is very appealing since it requires sunlight as the only energy input. However, the development of highly selective and efficient photocatalysts is still very challenging. It has been reported that CO_2 can be spontaneously activated on gallium nitride (GaN). Moreover, the photocatalytic activity for CO_2 conversion into methanol can be drastically enhanced by incorporating a small amount of Mg dopant. In this work, density functional theory (DFT) based on a cluster model approach has been applied to further explore the photocatalytic activity of bare GaN towards CO_2 adsorption and conversion. We extended the investigation of Mg-doping replacing one Ga atom with Mg on three different sites and evaluated the consequent effects on the band gaps and CO_2 adsorption energies. Finally, we explore different routes leading to the production of methanol and evaluate the catalytic activity of bare GaN by applying the energetic span model (ESM) in order to identify the rate-determining states which are fundamental for suggesting modifications that can improve the photocatalytic activity of this promising material.

Introduction

The chemical transformation of carbon dioxide (CO_2) into chemicals and fuel has been receiving growing attention since it can potentially mitigate the negative environmental impact of increasing greenhouse gas emissions in the atmosphere and furnish a new renewable carbon source.[1–7] In previous studies, we focused on homogeneous catalytic CO_2 conversion to cyclic carbonates[8,9] and methanol[10] using sustainable alkali halide–glycol complexes and Ru-complexes, respectively. Recently, our focus has been on photochemical CO_2 reduction since it requires sunlight as the only energy input. Significant attention has been paid to this subject in recent years, and substantial advances in the hydrogenation of CO_2 to hydrocarbons and oxygenates have been achieved. Among these products, methanol is one of the most desired since it can be used as a liquid fuel-like renewable energy source and a chemical feedstock for other useful chemicals. Due to the high thermodynamic stability of the CO_2 molecule, the first step of its reduction involves the adsorption and its consequent activation on the photocatalyst surface.

Various semiconductor photocatalysts, including oxides, oxynitrides, sulfides, and phosphides, have been investigated over the last few decades.[11–18] It has been observed that the presence of oxygen vacancies in metal oxide surfaces dominates the CO_2 adsorption.[19,20] However, this adsorption is hindered by the adsorption of O_2, which occupies the vacancies leading to an inactive surface. Moreover, metal oxide semiconductors generally exhibit a large band gap, which limits the absorption of the visible and infrared solar spectrum. Therefore, it is of both fundamental and practical interest to explore alternative photocatalysts that can harvest a large part of the solar spectrum and can lead to spontaneous activation of the CO_2 molecule.

In this regard, the thermodynamically stable wurtzite-structure gallium nitride (GaN) has been proposed as a promising material for the reduction of highly stable CO_2 molecules due to its unique electronic and optical properties. GaN has a wide band gap of 3.4 eV which can be tuned to absorb nearly the entire solar spectrum by alloying it with In and Al. Mi and collaborators[21] have demonstrated the photochemical reduction of CO_2 to CH_3OH, CO, and CH_4 with sunlight by a joint experimental and computational study based on periodic boundary condition (PBC) calculations. The authors also discovered that, with the incorporation of Mg dopant, the rate of CO_2 reduction to CH_3OH, CH_4, and CO is enhanced nearly 50-fold due to the reduced surface potential barrier and the enhanced adsorption of CO_2 molecules on the surface of the nanowire. In a very recent study, Liu and co-workers[22] demonstrated that bulk GaN

[a] *CEITEC – Central European Institute of Technology, Brno University of Technology, Purkyňova 123, Brno 612 00, Czech Republic. E-mail: butera@vutbr.cz*

[b] *Center for Micro- and Nanostructures & Institute of Solid State Electronics, TU Wien, 1040 Vienna, Austria*

This journal is © The Royal Society of Chemistry and the Chinese Chemical Society 2021

is an efficient catalyst for the selective direct hydrogenation of CO_2 to DME, and DME was rigorously revealed as the primary product. The authors have performed DFT calculations using PBC methods in order to investigate the details of the reaction conversion mechanism. According to the authors, the reaction proceeds through the formation of adsorbed H_2COH^* species which can be hydrogenated to methanol or dissociate to CH_2^* and OH^*. The energy barrier involved in the former process is calculated to be ~ 1 eV, which is higher than the latter. Their DFT results well explain why DME rather than methanol is formed as the primary product on GaN surfaces, *i.e.* the difficult hydrogenation of CH_2OH^* to CH_3OH^* and the unfavourable formation of CH_3O^*. The CO_2 photoreduction to hydrocarbons requires the presence of H^+ species which can be formed by water oxidation on GaN surfaces or *via* the dissociation of hydrogen molecules (H_2). In this regard, the hydrogen evolution reaction[23–26] represents a competing reaction.

Calculations based on a cluster model approach have some advantages over PBC methods, such as the use of hybrid functionals at a lower computational cost, that allows for a highly accurate description of electronic properties; the ability to add/subtract a charge carrier without suffering from inter-actions with similar charge carriers due to periodic boundary conditions,[27,28] which makes cluster approaches suitable for the study of charged systems. Thanks to the reduced size, a cluster approach can be used to intercept all the stationary points, including the more complex transition states, involved in the catalytic cycle and to determine the rate determining states.[29–31] On the other hand, a PBC approach allows for the investigation of extended surfaces and provides an accurate description of the structural properties of the surface and molecular adsorbates. The complementarity of the two computational methods can therefore lead to an in-depth understanding of the structure–property relationship.[32]

In this work, we have used DFT calculations based on a cluster model approach in order to further explore the photo-catalytic activity of bare GaN towards CO_2 conversion. Based on the findings reported by Mi and collaborators,[21] we have extended the investigation of Mg-doping replacing one Ga atom with Mg on three different sites and evaluated the consequent effects on the band gaps and CO_2 adsorption energies. This provides a more realistic picture of the stochastic distribution of dopant atoms within the crystal and on its surface. Based on the results published by Liu and co-workers,[22] we have explored different routes leading to the production of methanol that could potentially involve lower energy barriers. The catalytic activity of bare GaN has been evaluated by applying the energetic span model (ESM)[33,34] in order to identity the rate-determining states and to suggest modifications that can improve the photocatalytic activity of this promising material. Eventually, the influence of Mg-doping at different sites on the catalytic CO_2 conversion into methanol has been investigated. As will be discussed in more detail in the next sections, the reliability of the selected cluster models has been confirmed by the good agreement of the geometric parameters, that include calculated bond distances and angles, compared to the ones

reported in ref. 21. Moreover, similar trends of the adsorption energies using the two different computational approaches have been computed, which further support the potential use of the selected cluster models to determine adsorption energies as a valid alternative to the more extended surfaces used in PBC calculations. The stability of the pure and Mg-doped GaN clusters has also been evaluated and the details are discussed in the ESI.† Therefore, these models can be used for further investigations allowing a better understanding of the photo-catalytic activity of GaN-based materials at a notably reduced computational cost.

Results and discussion

GaN cluster selection and CO_2 adsorption

Two different cluster models have been selected in this study: **A_GaN** built up of three Ga–N moiety rows and 2 layers for a total number of 58 atoms; **B_GaN**, including four Ga–N moiety rows and three layers (112 atoms). Both the optimized structures are shown in Fig. 1. For the sake of simplicity, throughout the text, all the structures labeled with "A" and "B" will refer to the smaller and bigger size cluster models, respectively, while "GaN" and "Mg" will be used to indicate the pristine and Mg-doped models, respectively. To identify the three different studied doping sites, the superscripts "surf", "FL" and "bulk" will be adopted to refer to the surface, first layer and bulk, respectively.

As the first step of our investigation, we have focused on the adsorption of CO_2 on the surface of both the cluster models. The relative adsorption energies, $E(CO_2)_{ads}$, are calculated as:

$$E(CO_2)_{ads} = E_{cluster+CO_2} - E_{cluster} - E_{CO_2} \qquad (1)$$

where $E_{cluster}$ is the energy of the optimized cluster, E_{CO_2} is the energy of the CO_2 molecule, and $E_{cluster+CO_2}$ is the energy of the cluster when the CO_2 molecule is coordinated to the surface. The linear CO_2 has therefore been added to both **A_GaN** and **B_GaN** at an initial distance of about 3 Å from the surface. In both the systems, during the relaxation, the CO_2 is spontaneously coordinated to the GaN surface *via* a single C–N bond and the consequent deformation of the O–C–O from the original angle of $180°$ to a bent conformation (see Fig. 1 and Table 1). The C coordination is also confirmed by NBO analysis which underlines the formation of a single bond between C and N2, with a higher contribution of the N hybrid orbitals (63%) with respect to the C hybrid orbitals (37%), as well as a higher polarization coefficient of N (0.80) than C (0.60). NBO analysis also shows the formation of a double bond between C and O1 and a single bond between C and O2. In **1B_GaN**, two O–Ga interactions are established between the negatively charged oxygen atoms O1 (−0.718) and O2 (−0.790) and the positive Ga1 (+1.740) and Ga3 (+2.123) atoms, respectively. As for **1A_GaN**, the interaction between O1 and Ga1 becomes stronger as underlined by the O1–Ga1 bond whose distance is 0.342 Å shorter than in **1B_GaN**. However, the O2–Ga3 bond distance is 0.712 Å longer. Overall, increasing the size of the cluster has little influence on the CO_2 adsorption mode as also shown by the selected geometric parameters reported in Table 1.
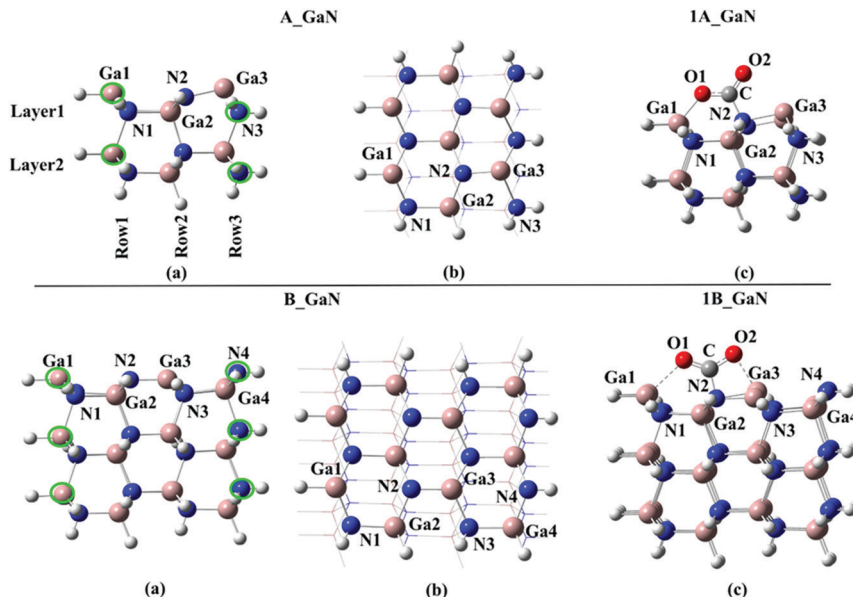
Fig. 1 Top: (a) side and (b) top view of the **A_GaN** cluster model and (c) **1A_GaN** intermediate; bottom: (a) side and (b) top view of the **B_GaN** cluster model and (c) **1B_GaN** intermediate.

Moreover, very similar adsorption energies of −2.11 and −2.05 eV have been calculated for the adsorption of CO_2 on **A_GaN** and **B_GaN**, respectively, whose optimized structures **1A_GaN** and **1B_GaN** are shown in Fig. 1c. Mi et al.[21] calculated an adsorption energy of 1.76 eV of one CO_2 molecule on GaN(100) using PBC calculations. As shown in Table 1, the geometric parameters computed by the authors are in good agreement with those obtained using our selected cluster models.

The effect of Mg-doping on the CO_2 adsorption energies has been evaluated on both the **A_GaN** and **B_GaN** models. Three different doping positions have been considered as shown in Fig. 2, while the corresponding adsorption energies are reported in Table 2. Mi et al.[21] computed an adsorption energy of −2.48 eV for CO_2 on the Mg-doped GaN surface. The doping site considered by the authors can be compared to our **A_Mg^{surf}** and **B_Mg^{surf}** systems, whose calculated adsorption energies are 3.23 and 3.12 eV for **1A_Mg^{surf}** and **1B_Mg^{surf}**, respectively. According to those results, our cluster models tend to over-estimate the adsorption energies giving more negative values. However, both the methods show a much stronger CO_2 adsorption energy in the presence of the Mg dopant which corresponds to
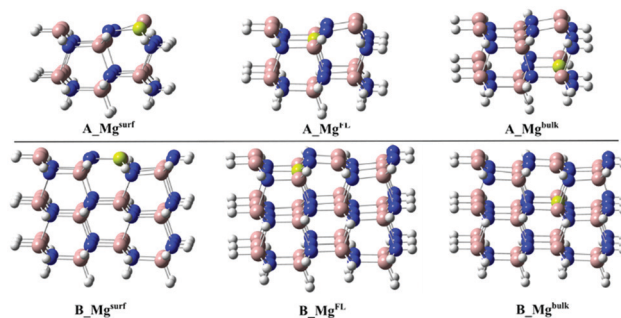
Fig. 2 Top: side view of the **A_Mg** cluster models doped by replacing one Ga atom of the surface (**A_Mg^{surf}**), first layer (**A_Mg^{FL}**) and bulk (**A_Mg^{bulk}**) with Mg. Bottom: side view of the **B_Mg** cluster models doped by replacing one Ga atom of the surface (**B_Mg^{surf}**), first layer (**B_Mg^{FL}**) and bulk (**B_Mg^{bulk}**) with Mg.

0.7 eV for the PBC calculations in ref. 21, and 1.1 eV for our cluster model calculations.

As shown in Table 2, the stronger adsorption of the CO_2 molecule in the presence of the Mg dopant is particularly enhanced when Mg replaces a gallium atom of the surface as in **A_Mg^{surf}** and **B_Mg^{surf}** in Fig. 2.

On the other hand, when Mg occupies a "bulk-like" position (**A_Mg^{bulk}** and **B_Mg^{bulk}** in Fig. 2), the calculated adsorption energy is much more similar to the undoped case. For a better understanding of the influence of Mg doping on the adsorption energy, the total adsorption energy, E_{ads}, of CO_2 on the B_Mg

Table 1 Adsorption energies (Ads energy) of CO_2 on **A_GaN** and B_GaN clusters, along with the main calculated geometric parameters. Values from ref. 21 are also shown for direct comparison

	A_GaN	**B_GaN**	Ref. 21
	B3LYP/6-31+G**	B3LYP/6-31+G**	PBC
Ads energy (eV)	−2.11	−2.05	−1.76
C–N2 (Å)	1.475	1.418	1.41
O1–Ga1 (Å)	1.918	2.323	2.24
O2–Ga3 (Å)	2.793	2.081	2.10
Ga1–N2–Ga3 (°)	170.4	167.0	
O1–C–O2 (°)	123.8	129.4	128.3

Table 2 Adsorption energies (eV) of CO_2 on **A_Mg** and **B_Mg** clusters, for the three studied doping sites

1A_Mg^{surf}	1B_Mg^{surf}	1A_Mg^{FL}	1B_Mg^{FL}	1A_Mg^{bulk}	1B_Mg^{bulk}
3.23	3.12	2.95	2.54	2.65	2.29

8208 | *Mater. Chem. Front.*, 2021, **5**, 8206–8217

This journal is © The Royal Society of Chemistry and the Chinese Chemical Society 2021

clusters has been decomposed into two main contributions, *i.e.*, interaction and distortion energies:

$$E_{ads} = E_{int} + E_{dist} \qquad (2)$$

The interaction energy, E_{int}, is given by the difference between the energy of the whole system and that of the single components taken at the final geometry of the adsorbed state, thus accounting for the bare electronic effects occurring at the adsorbate–surface interface:

$$E_{int} = E_{system} - \left(E^*_{adsorbate} + E^*_{surface}\right) \qquad (3)$$

The distortion energy, E_{dist}, is given by eqn (4):

$$E_{dist} = E^*_{adsorbate} + E^*_{surface} - E_{adsorbate} - E_{surface} \qquad (4)$$

where the terms with and without the * are taken, respectively, at the geometry of the final adsorbed state and the unperturbed equilibrium structures of each single component. This contribution accounts for the structural arrangements of both molecule and surface occurring upon adsorption.

As seen in Table 3, a positive contribution of about 4 eV, due to the distortion of the bare and Mg-doped GaN as a consequence of the CO_2 adsorption, has been calculated. Moreover, the positive deformation energy confirms also that the CO_2 molecule is activated upon coordination, changing from a linear structure to a bent one. On the other hand, the very negative terms of the interaction energy indicate a strong interaction between the CO_2 molecule and the surface favoring the overall adsorption process. Particularly, following the same trend of the adsorption energy, the interaction energy becomes stronger when the cluster models are doped with Mg, and a more negative interaction energy is calculated when Mg replaces a surface Ga atom as in **1B_Mg^{surf}**, while a more positive value is obtained for the "bulk-like" replacement. Therefore, the replacement of Mg on the surface will lead to a stronger interaction energy and an overall stronger adsorption energy.

Table 3 Calculated E_{int} and E_{dist} contributions to the CO_2 adsorption energy on the pristine **B_GaN** and B_Mg cluster models. Energies are given in eV

1B_GaN		1B_Mgsurf		1B_MgFL		1B_Mgbulk	
E_{int}	E_{dist}	E_{int}	E_{dist}	E_{int}	E_{dist}	E_{int}	E_{dist}
−5.94	3.89	−6.95	3.83	−6.63	4.10	−6.22	3.93

Table 4 Methanol adsorption energies, E, (eV) on the pristine **A_GaN** and **A_Mg** cluster models along with the calculated Ga−O distance (Å)

	A$_{MeOH}$_GaN	A$_{MeOH}$_Mg^{surf}	A$_{MeOH}$_Mg^{FL}	A$_{MeOH}$_Mg^{bulk}
E	−1.69	−1.52	−1.53	−1.54
Ga–O	2.009	2.006	2.012	2.013

Methanol production: The adsorption energies of one methanol molecule on the selected cluster models have been calculated and the corresponding values are reported in Table 4. Thanks to the agreement between the small and big cluster models on the computed CO_2 adsorption energies, only the small clusters have been considered.

These values show that the adsorption of the methanol molecule is less strong (more positive) than that of CO_2 for the bare and Mg-doped clusters. However, the methanol adsorption energy on **A_GaN** is slightly higher than the Mg-doped cases. The adsorption mode of the methanol molecule on the GaN is not particularly influenced by the Mg doping. Moreover, very similar adsorption energies have been calculated for the Mg-doping at the three different sites (see Table 4). Our calculations show that the adsorption of CO_2 on pristine **A_GaN** is 0.42 eV stronger than that of methanol (see Tables 1 and 4). This difference increases when the Mg-doped clusters are taken into account and it becomes 1.71, 1.42 and 1.11 eV (see Tables 2 and 4) for **A_Mg^{surf}**, **A_Mg^{FL}** and **A_Mg^{bulk}**, respectively. In other words, replacing one Ga atom with Mg favors the CO_2 adsorption (particularly when a surface Ga atom is replaced) but has no influence on the methanol adsorption facilitating its release.

Band gaps and HOMO/LUMO orbitals

For all six Mg-doped and two bare GaN clusters, the band gaps have been calculated as the energy difference between the Lowest Unoccupied Molecular Orbital (LUMO) and Highest Occupied Molecular Orbital (HOMO). The computed band gap of the pristine **B_GaN** is 3.5 eV which is very similar to the experimental one (3.4 eV). According to our results, reported in Table 5, the presence of Mg lowers the band gap. This effect is much enhanced when Mg replaces a surface Ga as in **B_Mg^{surf}**. Even though the smaller **A_GaN** and **A_Mg** models dramatically underestimate the band gaps, the obtained trend confirms that calculated with the bigger cluster model.

The band gaps can also be derived from the gap between the photoemission (PES) and inverse-photoemission (IPES) energy levels.[27,35] It is indeed possible to compute the electron affinity/ionization potential of pristine and Mg-doped GaN by the addition/removal of an electron from the neutral system. This would be analogous to the measurement of the fundamental gap arising from the PES/IPES process, as explained in more detail in the ESI.† By applying this method to the smaller cluster models, **A_GaN** and **A_Mg^{surf}**, we obtain band gap values of 2.86 and 2.27 eV, respectively. Even though these values still underestimate the band gaps, they give more realistic values showing that the smaller clusters can be used for qualitative analysis at a very reduced computational cost.

Table 5 Band gaps of all the selected clusters calculated as the difference between the HOMO and LUMO orbitals. Energies are given in eV

A_GaN	B_GaN	A_Mg^{surf}	B_Mg^{surf}	A_Mg^{FL}	B_Mg^{FL}	A_Mg^{bulk}	B_Mg^{bulk}
1.24	3.52	0.59	2.49	1.13	3.29	1.15	3.27
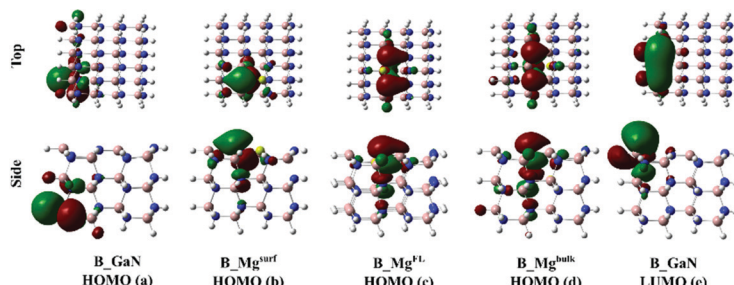
Fig. 3 Top and side view of the HOMO orbitals of **B_GaN** (a), **B_Mg^{surf}** (b), **B_Mg^{FL}** (c) and **B_Mg^{bulk}** (d); top and side view of the LUMO orbital of the pristine **B_GaN** (e).
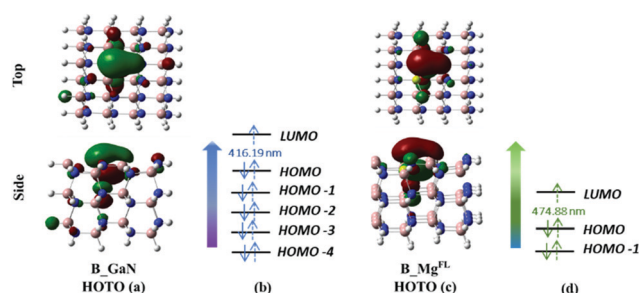

Fig. 4 Top and side view of the HOTO of **B_GaN** (a) and **B_Mg^{FL}** (c) cluster models; canonical orbitals involved in the transition to the first excited state of **B_GaN** (b) and **B_Mg^{FL}** (d).

Fig. 3 shows the HOMO orbitals of the **B_GaN** and **B_Mg** clusters. The HOMO orbital of the pristine GaN is localized on the bottom-left part of the cluster. On the other hand, when the surface Ga atom is replaced with Mg, as in **B_Mg^{surf}**, the HOMO orbital involves mostly the atoms of the surface layer. A more extended character of the HOMO orbital is calculated in the case of Mg-doping as in **B_Mg^{FL}** and **B_Mg^{bulk}**. The analysis of the LUMO orbitals, instead, shows a very similar character of the LUMO for all the studied clusters. For this reason, in Fig. 4 only the undoped case is shown.

Therefore, both the "**A**" and "**B**" cluster models have underlined the spontaneous coordination of the CO_2 molecule on the pristine and Mg-doped surfaces and its consequent activation is thanks to the formation of a strong C–N single bond. Moreover, both the "**A**" and "**B**" clusters confirm that replacing a surface Ga atom with Mg leads to stronger (more negative) adsorption and interaction energies, along with notably reducing the band gap.

Absorption spectra

TD-DFT, which is a popular tool for computing the electronic excitation energies and the properties related to the optical spectra,[36–38] has been used to investigate the light absorption of pure and Mg-doped GaN materials determining their vertical electronic absorption energies of optical transitions. The corresponding simulated spectra are shown in the ESI,† while the main excitation energies and the related oscillator strengths are listed in Table 6.

We report all excitations falling in the energy interval in terms of wavelengths between ∼700–350 nm (corresponding to ∼1.8–3.5 eV). This energy interval includes the visible spectrum (400–700 nm). The main difference between pristine and Mg-doped clusters is that the inclusion of Mg leads to absorption features at lower energies and this effect is particularly evident for the **B_Mg^{surf}** cluster which includes a Mg surface atom: pure GaN shows peaks that are located at about 3 eV, which means ∼400 nm in the visible region of violet light, and some further peaks are present out of the visible window (less than 400 nm); on the other hand, the presence of Mg shifts the absorption up to 666.32 nm, extending the range of the absorption of visible light and, consequently, improving the photocatalytic performance of gallium nitride.

The analysis of the TD-DFT calculations underlines that in the first excited state for both **B_Mg^{surf}** and **B_Mg^{bulk}** the HOMO–LUMO transition dominates with a transition coefficient of about 0.70. In the case of **B_Mg^{FL}**, two transitions are involved: the HOMO−1 → LUMO and HOMO → LUMO, with transition coefficients of 0.6 and 0.4, respectively (see Fig. 4d). Eventually, in the **B_GaN** cluster, several transitions contribute to the first excited state with very similar coefficients (see Fig. 4b). In these two latter cases, examining the relevant canonical orbitals is not

Table 6 Main excitation energies (eV and nm) and related oscillator strengths (f) for the first five excited states of the **B_GaN** and **B_Mg** cluster models calculated with the TD-DFT method

	B_GaN			**B_Mg^{surf}**			**B_Mg^{FL}**			**B_Mg^{bulk}**		
	eV	nm	f	eV	nm	f	eV	nm	f	eV	nm	f
ES1	2.98	416.2	0.0143	1.86	666.3	0.0033	2.61	474.9	0.0135	2.63	471.6	0.0237
ES2	3.06	405.7	0.0114	2.36	525.6	0.0446	2.67	463.5	0.0167	2.71	456.8	0.0018
ES3	3.08	402.1	0.0020	2.65	467.2	0.0102	2.85	434.7	0.0118	2.88	429.7	0.0036
ES4	3.25	381.8	0.0038	2.68	461.8	0.0050	2.92	425.1	0.0061	2.95	420.1	0.0115
ES5	3.28	377.6	0.0006	2.70	458.9	0.0217	2.95	419.9	0.0040	3.00	412.7	0.0188

8210 | *Mater. Chem. Front.*, 2021, **5**, 8206–8217

This journal is © The Royal Society of Chemistry and the Chinese Chemical Society 2021

particularly helpful and therefore the analysis of the Natural Frontier Orbitals (NTOs) has been performed and the corresponding Highest Occupied Transition Orbitals (HOTOs) are shown in Fig. 4a and c for **B_GaN** and **B_Mg^{FL}**, respectively.

CO_2 conversion on A_GaN

As the first step of our investigation of the CO_2 conversion into methanol, we have considered the coordination of: (a) a CO_2 molecule followed by the coordination of a hydrogen molecule (mechanism 1, Fig. 5) and (b) a hydrogen molecule followed by CO_2 (mechanism 2, Fig. 6). For a direct comparison with the adsorption energy given in the previous section, the electronic energies calculated at B3LYP/6-31+G** will be discussed while comparing the reaction mechanisms. However, free energies are also reported in the Potential Energy Surfaces (PESs) and they will be discussed in more detail in the next section where the energetic span model will be applied in order to identify both the rate-determining intermediate, TDI, and the rate-determining transition state, TDTS.

Mechanism 1. As mentioned in the previous section, the addition of a CO_2 molecule to **A_GaN** leads to its spontaneous

coordination to the surface through the C–N1 bond as in **1A_GaN**, which lies at 2.11 eV below the reaction coordinate. When a hydrogen molecule is added to **1A_GaN** to form **2A_GaN**, no spontaneous adsorption is observed and the calculated H_2-Ga bond distance is 2.573 Å. The reaction can proceed *via* **TS2A_GaN** in which the calculated imaginary frequency of $-1032.54i$ cm^{-1} is associated with the breaking of the H–H bond and the consequent formation of the O–H and Ga–H bonds, as shown in **3A_GaN**. The energy barrier is 0.4 eV with respect to the previous intermediate. The second transition state, **TS2A_GaN**, involves a hydride nucleophilic attack at the carbon atom and breaking of the C–OH bond. The calculated energy barrier with respect to **3A_GaN** is 2.9 eV. The IRC calculations show that in the subsequent intermediate, **4A_GaN**, the HCO group is rotated in order to form an O–Ga bond, while the OH group is transferred to the adjacent Ga surface atom. This intermediate is calculated to be ~1 eV more stable than the previous one. A second uncoordinated molecule of H_2 is added to the system as in **5A_GaN** and it is heterolytically broken as shown by the imaginary frequency of $-1094.62i$ cm^{-1}
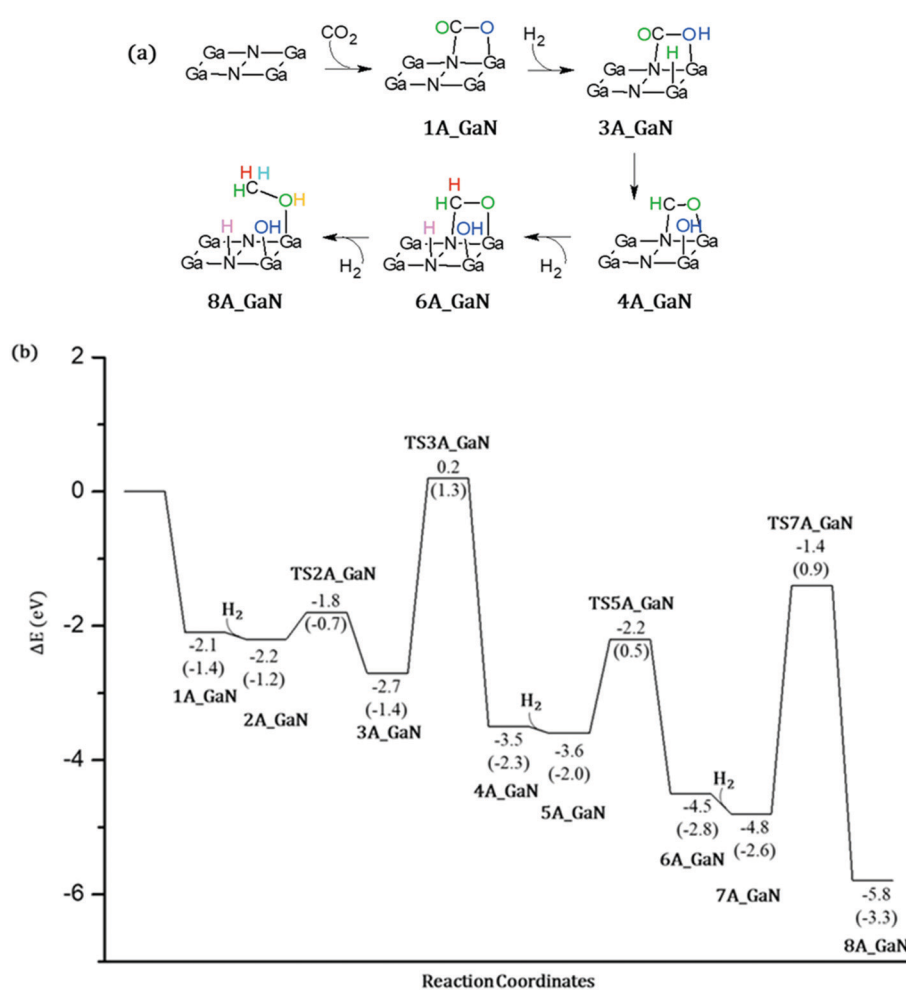
Fig. 5 (a) Schematic representations of all the intercepted stationary points along with the (b) calculated B3LYP energy profile for the CO_2 conversion to methanol on the **A_GaN** cluster model according to mechanism 1. Energies are in eV and relative to the asymptote of the reactant. Free energies (eV) are shown in parentheses.
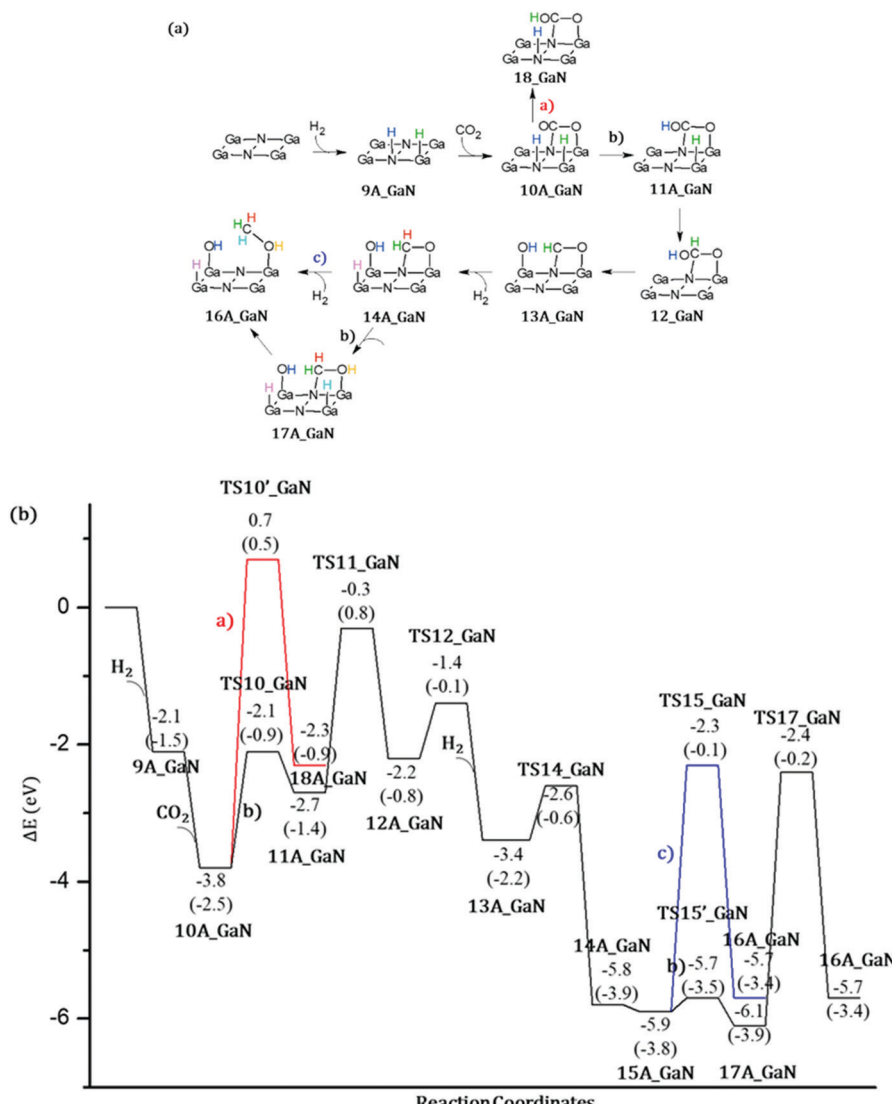
Fig. 6 (a) Schematic representations of all the intercepted stationary points along with the (b) calculated B3LYP energy profile for the CO$_2$ conversion to methanol on the **A_GaN** cluster model according to mechanism 2. Energies are in eV and relative to the asymptote of the reactant. Free energies (eV) are shown in parentheses.

calculated in **TS5_GaN**. The overcoming of an energy barrier of 1.3 eV leads to the formation of the **6A_GaN** intermediate in which a N–H bond and a C–H bond are formed. In this intermediate, the carbon atom of the H$_2$C–O* species coordinates to a surface nitrogen atom via a sp^3 carbon with a calculated bond distance of 1.572 Å, while the oxygen atom binds to a surface Ga atom via a Ga–O bond of 1.868 Å. The C–O bond is 1.409 Å which is longer than a C=O double bond. Therefore, these results show that this mechanism does not lead to the formation of acetaldehyde. Eventually the third molecule of hydrogen is added to the system which remains uncoordinated as in **7A_GaN**. The last transition state, **TS7_GaN**, of the proposed mechanism involves the hydrogenation of the coordinated H$_2$CO thanks to the breaking of the H–H bond and the formation of both CH and OH. The calculated imaginary frequency is −1307.49i cm^{-1} and the involved activation barrier with respect to **7A_GaN** is 3.44 eV. Eventually, the **8A_GaN** intermediate is formed in which the

methanol molecule is coordinated via a Ga–OH bond whose calculated distance is 1.951 Å, while a hydrogen bond is also formed between the hydrogen of the methanol and the oxygen of the adsorbed OH, whose distance is 1.423 Å. This intermediate lies at 4.4 eV below the reaction asymptote.

Mechanism 2. As seen before, when a H$_2$ molecule is added to **1A_GaN**, neither spontaneous molecular nor dissociative adsorption is observed. Moreover, no transition state associates to the coordination of H$_2$ or its dissociation and further coordination has been intercepted. On the other hand, our calculations show that when the H$_2$ molecule is added to the **A_GaN** in the absence of the coordinated CO$_2$, it spontaneously gives dissociative adsorption leading to the formation of N–H and Ga–H bonds as in **9A_GaN**, which lies at 2.08 eV below the reactants' asymptote. Liu and co-workers[22] have performed PBC calculations showing that H$_2$ molecules dissociate at Ga–N pairs in a heterolytic pathway with low activation barriers of

0.09 eV on GaN(100). The different result can be associated to the higher reactivity of cluster models in comparison with PBC calculations. However, both the approaches underline the ease of the hydrogen adsorption process. Our calculations show that **9A_GaN** is almost isoenergetic with **1A_GaN** and therefore there is no preference in the adsorption of one molecule over the other as the first step of the reaction mechanism. This result was also confirmed by Liu and collaborators,[22] who underlined that the comparable adsorption of H_2 and CO_2 paves the way for the facile hydrogenation of CO_2 on the catalyst surface. The presence of the adsorbed hydrogen atoms on the GaN cluster does not prevent the further coordination, and consequent activation, of the approaching CO_2 molecule. Indeed, our calculation shows that when the linear inactivated molecule of CO_2 is added to **9A_GaN** at an initial C–N1 distance of 2.710 Å, during the optimization it coordinates as described in **1A_GaN**, leading to the formation of the intermediate **10A_GaN** which is found to be 1.68 eV more stable than the previous intermediate. From **10A_GaN**, the reaction can proceed *via* two different routes: (a) proton transfer from the surface nitrogen to the oxygen of the activated CO_2 (**TS10_GaN**); (b) nucleophilic attack at the activated carbon of CO_2 by the hydride bound to the surface Ga atom (**TS10′_GaN**). The former transition state is found to be 1.47 eV more stable than the latter, with a calculated activation energy of 1.62 eV with respect to **10A_GaN**. This result is also in agreement with those reported by Liu and co-workers[22] who report that the hydrogenation of CO_2 to COOH* is more favorable than that to HCOO. The formed intermediate **11A_GaN** is 2.66 eV more stable than the separated reactants. The reaction proceeds *via* **TS11_GaN** in which the hydride attacks the electrophilic carbon coordinated to the surface nitrogen as underlined by the imaginary frequency of $-1235.38i$ cm^{-1}. In the formed intermediate, **12A_GaN**, the carbon atom shows sp^3 hybridization which involves a single bond with the previously formed OH group, a second single bond with the transferred hydrogen, a third single bond with the second oxygen of the original CO_2 molecule, and eventually a fourth single bond with the surface nitrogen atom. Once the intermediate **12A_GaN** is formed, two different routes have been explored: (a) the former consists of the addition of a further molecule of hydrogen whose H–H bond breaks forming Ga–H and O–H bonds. As will be discussed in more detail in the ESI,† following this route which involves **TS12′_GaN**, we did not succeed in intercepting the final transition state leading to the formation of methanol; (b) the latter involves the breaking of the C–OH bond which is broken *via* **TS12_GaN** by overcoming an energy barrier of 0.72 eV with respect to **12A_GaN**, and leads to the formation of **13A_GaN** in which the OH group is transferred to the next Ga surface atom, while the carbon atom gets back to sp^2 hybridization. As seen for **1A_GaN**, when a second molecule of hydrogen is added to **13A_GaN**, it does not spontaneously coordinate to the surface. Three different mechanisms have been considered. We will describe the details of the selected one in this section while the details of the other two routes can be found in the ESI.† The H–H bond of the uncoordinated H_2 molecule is broken *via* TS13_GaN: one hydrogen atom adsorbs on the GaN surface

while the second binds the carbon atom forming the intermediate **14A_GaN**, in which the H_2C–O species coordinates to a surface nitrogen atom in a similar way as seen for the 6A_GaN intermediate and no acetaldehyde is formed. These results support the experimental findings based on which no acetaldehyde was observed. The calculated imaginary frequency is $-520.83i$ cm^{-1}, while the activation barrier is 0.8 eV with respect to **14A_GaN**. Also in this case, the addition of a further hydrogen molecule to the reaction system does not lead to its spontaneous adsorption and the molecule is kept at a distance of ~2.600 Å from the surface as in intermediate **15A_GaN**. From this intermediate, two different mechanisms can occur which can be defined as (a) concerted and (b) step-wise mechanisms. The concerted mechanism consists of the direct hydrogenation of the adsorbed H_2C–O species *via* the final TS15_GaN whose imaginary frequency is $-1284.50i$ cm^{-1} and which involves the highest activation energy of 3.63 eV. The last intermediate **16A_GaN** lies at 5.70 eV below the reactants' asymptote and shows that the methanol molecule coordinates to a surface Ga atom whose calculated bond distance is 2.000 Å, along with a hydrogen atom adsorbed on a second surface Ga with a computed distance of 1.593 Å and eventually a Ga–OH bond of 1.793 Å. In the step-wise mechanism the added uncoordinated hydrogen molecule first breaks forming O–H and Ga–H bonds *via* **TS15′_GaN** with a very low activation energy of 0.17 eV and forming the intermediate **17A_GaN** that lies at 2.44 eV below the separated reactants. In the last step, a C–H bond is formed through **TS16_GaN** which involves an energy barrier of 3.70 eV.

It is important to note that the stabilization energies of the last intermediates (**8A_GaN** and **16A_GaN**) of the proposed catalytic cycles are much more negative than the ones discussed in the previous section (A_{MeOH}_GaN and A_{MeOH}_Mg). Since the adsorption mode of the methanol molecule is the same, the more negative stabilization energies are due to the presence of more adsorbed species in the former case. Therefore, in order to get a more realistic view, the coverage effect should be investigated on a more extended surface, which will be the focus of our further investigation.

Energetic span model and rate determining states: According to the energetic span model (ESM), the turnover frequency (TOF) can be derived from electronic-structure calculations by identifying the energetic span of the cycle, δE, which is defined as the energy difference between the points of highest and lowest energy along the reaction profile corresponding to the complete catalytic cycle. Kozuch and Shaik[33] extended this model including the ΔG_r of the reaction and defining δE_{ij} as:

$$\begin{cases} \delta E_{ij} = G(TS)j - G(I)i & j > i \\ \delta E_{ij} = G(TS)j - G(I)i - |\Delta G_r| & j \leq i \end{cases}$$

Therefore, if the j-th transition state lies after the i-th intermediate, then δE_{ij} is just the energy difference between them; if the j-th transition state precedes the i-th intermediate, then δE_{ij} is their energy difference minus the ΔG_r. The highest δE_{ij} corresponds to the energy span of the cycle connecting the

TOF-determining intermediate (TDI) and the TOF-determining transition state (TDTS). By applying this method to the potential energy surface of Fig. 5 and considering the free energies given in parentheses, we can identify **6A_GaN** as the TDI and **TS5A_GaN** as the TDTS with a corresponding δE of 3.7 eV. Therefore, the rate determining state involves the last hydrogenation for the production of methanol. The same δE, involving very similar structures of TDI and TDTS, is calculated when the (c) route of the potential energy surface in Fig. 6 is considered. Along the (b) route, the application of the ESM leads to the identification of the rate-determining states, which involve the formation of the third C–H bond and the consequent production of methanol. Therefore, our calculations show that the last step leading to the methanol formation is the most challenging. Interestingly, no difference in terms of energy barrier has been found between the hydrogenation of the adsorbed H_2CO species with an approaching inactivated hydrogen molecule, and the transfer of an adsorbed hydrogen atom. This is due to the very strong bonds that the adsorbed species establish with the GaN surface atoms that prevent easy bond breaking/formation. The application of the ESM to the mechanism proposed by Liu and collaborators[22] leads to a δE of 3.3 eV. In their investigation, the TDI is the intermediate in which the CO_2 molecule is activated on GaN as the bent COO* species while H_2 is adsorbed dissociatively on Ga–N Lewis pairs (an intermediate that can be compared to our **10A_GaN**). The TDTS of the catalytic cycle proposed by Liu and collaborators[22] is the transition state associated to the C–H bond formation *via* an adsorbed hydrogen transfer to the H_2COH* (comparable to **TS17_GaN**). Therefore, their study also identifies the last step of the methanol production as the rate-determining state. The authors indeed suggest that the dissociation of CH_2OH* into CH_2* (which is further hydrogenated to CH_3*) and OH* is significantly more favorable than the formation of methanol, explaining why their experimental findings show that methanol is not the primary product of the CO_2 hydrogenation.

Even though we were not able to identify an alternative mechanism for the methanol production involving lower energy barriers, our investigation furnishes a wider picture of the possible conversion route which contributes to a deeper understanding of the complex reaction mechanism. Moreover, the application of the ESM allows us to identify the rate determining states which is key information for the development of catalysts with improved performances.

Experimental

All the calculations have been performed using a cluster model approach. Two cluster models of 58, **A_GaN**, and 112, **B_GaN**, atoms have been carved out from the crystallographic structure of wurzite GaN, cutting along the (100) plane. We retained the cluster's overall zero spin and neutral charge by passivating with capping H atoms only those dangling bonds of our cluster that would have formed covalent bonds to Ga or N atoms in a bulk surface structure. The capping H atoms along with the outermost N and Ga atoms, underlined in green in Fig. 1, have

been kept fixed while the rest of the atoms were allowed to relax. These optimizations were performed at the B3LYP[39] level of theory as implemented in the Gaussian 16 quantum chemistry package[13,40] and using the LANL2DZ[14,41] pseudo potential for Ga atoms and the fully electron basis sets 6-31G for N and H. To check the accuracy of the selected computational protocol, preliminary tests were performed using the more accurate double hybrid PBE0DH[15,42] functional that combines exact HF exchange with an MP2-like correlation to a DFT calculation. Moreover, the Counterpoise error as implemented in Gaussian 16 software has been evaluated. These results, whose details can be found in the ESI,† have confirmed the reliability of the B3LYP functional, which was therefore selected in our study. Frequency calculations have been done to check the nature of the stationary points (minimum and transition state). In order to obtain more accurate adsorption energy values, single-point calculations using the more extended 6-31+G** basis sets, except for Ga, on the fully optimized geometry, have also been performed and the obtained energies will be discussed throughout the text (unless differently specified). To evaluate the influence of Mg on CO_2 adsorption, we replaced the three-coordinated Ga(+3) atom on the surface of the pristine **A_GaN** and **B_GaN** cluster models by Mg(+2), leading to the formation of **A_Mg** and **B_Mg** clusters, whose net charge is −1.

Conclusions

In this work, DFT calculations based on a cluster model approach have been used to explore the photocatalytic activity of bare GaN towards CO_2 conversion. Two different cluster models have been selected: **A_GaN** built up of three Ga–N moiety rows and 2 layers for a total number of 58 atoms and **B_GaN**, including four Ga–N moiety rows and three layers (112 atoms). We extended the investigation of the Mg-doping effect considering three different doping sites. Our calculations have shown that the CO_2 molecule spontaneously coordinates on the pristine and Mg-doped surfaces for both the selected cluster models. This coordination implies the consequent activation of CO_2 thanks to the formation of a strong C–N single bond and the change from the CO_2 linear structure to a bent one. The activation of the CO_2 molecule upon coordination is also confirmed by a similar positive contribution of about 4 eV for all the investigated cases related to its deformation along with the distortion of the bare and Mg-doped GaN clusters as a consequence of the CO_2 adsorption. On the other hand, both the clusters confirm that replacing a surface Ga atom with Mg leads to stronger (more negative) adsorption and interaction energies. The most negative interaction energy is calculated when Mg replaces a surface Ga atom as in **1B_Mg^{surf}**, while the more positive values are obtained for the "bulk-like" replacement. Therefore, the replacement of Mg on the surface leads to a stronger interaction energy and an overall stronger adsorption energy.

Small pristine **A_GaN** and Mg-doped **A_Mg** clusters have been used to calculate the adsorption energies of one molecule of methanol which is the final product of the catalytic cycle.

8214 | *Mater. Chem. Front.*, 2021, **5**, 8206–8217

This journal is © The Royal Society of Chemistry and the Chinese Chemical Society 2021

The calculated values have shown that the adsorption of a methanol molecule is less strong (more positive) than that of CO_2 with the bare **A_GaN** showing a stronger MeOH adsorption energy. The adsorption mode of the methanol molecule on GaN is not particularly influenced by the Mg doping and doping sites, as underlined by the very similar calculated adsorption energies. The highest difference between CO_2 and the MeOH adsorption energy of 1.71 eV was calculated when the two molecules were adsorbed on the **A_Mg^{surf}** cluster. Therefore, our calculations show the important contribution of replacing one surface Ga atom with Mg, which favors the CO_2 adsorption and its consequent activation, but has no influence on the methanol adsorption facilitating its release.

Using the bigger cluster models, the band gaps have been calculated as the difference between the HOMO/LUMO orbital energies. The calculated band gap of 3.52 eV obtained for the pure **B_GaN** cluster is in good agreement with the experimental band gap (3.4 eV). Our calculations show that Mg-doping contributes to decrease the band gaps and this effect is particularly important in the case of **B_Mg^{surf}** for which a band gap value of 2.49 eV has been calculated. On the other hand, the small cluster models tend to drastically underestimate the band gaps even though they confirm the trend and, therefore, they could be used for a qualitative analysis.

TD-DFT has been used to calculate the vertical electronic absorption energies at optical wavelengths for the pure and Mg-doped GaN model clusters. The main difference between pristine and Mg-doped clusters is that the inclusion of Mg leads to absorption features at lower energies and this effect is particularly evident for the **B_Mg^{surf}** cluster which includes a Mg surface atom: pure GaN shows peaks that are located at about 3 eV, which means $\sim$400 nm in the visible region of violet light, and some further peaks are present out of the visible window (less than 400 nm); on the other hand, the presence of Mg shifts the absorption up to 666.32 nm extending the range of the absorption of visible light and, consequently, improving the photocatalytic performance of gallium nitride.

Thanks to the agreement of the two size cluster models, the smaller and less computationally demanding **A_GaN** was selected for the investigation of CO_2 conversion into methanol. The catalytic activity of bare GaN was evaluated by applying the energetic span model in order to identify the rate-determining states. Following the proposed mechanism 1, the rate determining state involves the last hydrogenation for the production of methanol with a computed δE of 3.7 eV. The same δE, involving very similar structures of TDI and TDTS, is calculated when the (c) route is considered. Along the (b) route the application of the ESM leads to the identification of the rate-determining states which involve the formation of the third C–H bond and the consequent production of methanol. Therefore, our calculations show that the last step leading to methanol formation is the most challenging.

Therefore, the selected cluster models can be used for further investigations allowing a better understanding of the photocatalytic activity of GaN-based materials at a notably reduced computational cost.

Author contributions

V. B. performed the DFT simulations and analysis. Both the authors contributed to the manuscript.

Conflicts of interest

There are no conflicts to declare.

Acknowledgements

Notes and references

1 B. Aurianblajeni, M. Halmann and J. Manassen, Photo-reduction of carbon-dioxide and water into formaldehyde and methanol on semiconductor-materials, *Sol. Energy*, 1980, **25**, 165–170.

2 D. Canfield and K. W. Frese, Reduction of carbon-dioxide to methanol on n-GaAs and p-GaAs and p-InP: Effect of crystal-face, electrolyte and current-density, *J. Electrochem. Soc.*, 1983, **130**, 1772–1773.

3 O. K. Varghese, M. Paulose, T. J. LaTempa and C. A. Grimes, High-rate solar photocatalytic conversion of CO_2 and water vapor to hydrocarbon fuels, *Nano Lett.*, 2009, **9**, 731–737.

4 J. R. Cabrero-Antonino, R. Adam and M. Beller, Catalytic reductive N-alkylations using CO_2 and carboxylic acid derivatives: Recent progress and developments, *Angew. Chem., Int. Ed.*, 2019, **58**, 2–21.

5 S. Kar, A. Goeppert and G. K. S. Prakash, Integrated CO_2 capture and conversion to formate and methanol: Connecting two threads, *Acc. Chem. Res.*, 2019, **52**, 2892–2903.

6 Q.-W. Song, Z.-H. Zhou and L.-N. He, Efficient, selective and sustainable catalysis of carbon dioxide, *Green Chem.*, 2017, **19**, 3707–3728.

7 S. Samanta and R. Srivastava, Catalytic conversion of CO_2 to chemicals and fuels: the collective thermocatalytic/photo-catalytic/electrocatalytic approach with graphitic, *Mater. Adv.*, 2020, **1**, 1506–1545.

8 V. Butera, N. Russo, U. Cosentino, C. Greco, G. Moro, D. Pitea and E. Sicilia, Computational insight on CO_2 fixation to produce styrene carbonate assisted by a single-

center aluminum(III) catalyst and quaternary ammonium salts, *ChemCatChem*, 2016, **8**, 1167.

9 V. Butera and H. Detz, Cyclic carbonate formation from epoxides and CO_2 catalyzed by sustainable alkali halide–glycol complexes: A DFT study to elucidate reaction mechanism and catalytic activity, *ACS Omega*, 2020, **5**(29), 18064–18072.

10 V. Butera and H. Detz, Hydrogenation of CO_2 to methanol by the diphosphine–ruthenium(II) cationic complex: A DFT investigation to shed light on the decisive role of carboxylic acids as promoters, *Catal. Sci. Technol.*, 2021, **11**, 3556–3397.

11 L. Wang, Y. Dong, T. Yan, Z. Hu, A. A. Jelle, D. M. Meira, P. N. Duchesne, J. Y. Y. Loh, C. Qiu, E. E. Storey, Y. Xu, W. Sun, M. Ghoussoub, N. P. Kherani, A. S. Helmy and G. A. Ozin, Black indium oxide a photothermal CO_2 hydrogenation catalyst, *Nat. Commun.*, 2020, **11**, 2432.

12 A. Fujishima and K. Honda, Electrochemical photolysis of water at a semiconductor electrode., *Nature*, 1972, **238**, 37–38.

13 M. Halmann., Photoelectrochemical reduction of aqueous carbon-dioxide on p-type gallium-phosphide in liquid junction solar-cells, *Nature*, 1978, **275**, 115–116.

14 T. Inoue, A. Fujishima, S. Konishi and K. Honda, Photo-electrocatalytic reduction of carbon dioxide in aqueous suspensions of semiconductor powders, *Nature*, 1979, **277**, 637–644.

15 R. Vogel, P. Hoyer and H. Weller, Quantum-sized PbS, CdS, Ag2S, Sb2S3, and Bi2S3 particles as sensitizers for various nanoporous wide-bandgap semiconductors, *J. Phys. Chem.*, 1994, **98**, 3183–3188.

16 S. N. Habisreutinge, L. S. Mende and J. K. Stolarczyk, Photo-catalytic reduction of CO_2 on TiO_2 and other semiconductors, *Angew. Chem., Int. Ed.*, 2013, **52**, 7372–7408.

17 Y. F. Xu, P. N. Duchesne and L. Wang, *et al.*, High-performance light-driven heterogeneous CO_2 catalysis with near-unity selectivity on metal phosphides, *Nat. Commun.*, 2020, **11**, 5149.

18 Y. Wang, Y. Tian, L. Yan and Z. Su, DFT study on sulfur-doped g-C_3N_4 nanosheets as a photocatalyst for CO_2 reduction reaction, *J. Phys. Chem. C*, 2018, **122**(14), 7712–7719.

19 S. Funk, B. Hokkanen, E. Johnson and U. Burghaus, Effect of oxygen vacancy sites on CO_2 adsorption dynamics: The case of rutile (1×1)-$TiO_{2(}110)$, *Chem. Phys. Lett.*, 2006, **422**, 461–465.

20 T. L. Thompson, O. Diwald and J. T. Yates, CO_2 as a probe for monitoring the surface defects on $TiO_2(110)$ – temperature programmed desorption, *J. Phys. Chem. B*, 2003, **107**, 11700–11704.

21 B. AlOtaibi, X. Kong, S. Vanka, S. Y. Woo, A. Pofelski, F. Oudjedi, S. Fan, M. G. Kibria, G. A. Botton, W. Ji, H. Guo and Z. Mi, Photochemical carbon dioxide reduction on Mg-doped Ga(In)N nanowire arrays under visible light irradiation, *ACS Energy Lett.*, 2016, **1**, 246–252.

22 C. Liu, J. Kang, Z.-Q. Huang, Y.-H. Song, Y.-S. Xiao, J. Song, J.-X. He, C.-R. Chang, H.-Q. Ge, Y. Wang, Z.-T. Liu and Z.-W. Liu, Gallium nitride catalyzed the direct hydrogenation of carbon dioxide to dimethyl ether as primary product, *Nat. Commun.*, 2021, **12**, 2305.

23 J. K. Nørskov, T. Bligaard, A. Logadottir, J. R. Kitchin, J. G. Chen, S. Pandelov and U. Stimming, Trends in the exchange current for hydrogen evolution, *J. Electrochem. Soc.*, 2005, **152**, J23–J26.

24 Y. Zhao, C. Chang, F. Teng, Y. Zhao, G. Chen, R. Shi, G. I. N. Waterhouse, W. Huang and T. Zhang, Defect-engineered ultrathin δ-MnO2 nanosheet arrays as bifunctional electrodes for efficient overall water splitting, *Adv. Energy Mater.*, 2017, **7**, 1700005.

25 Y. Zhao, S. Zhang, R. Shi, G. I. N. Waterhouse, J. Tang and T. Zhang, Two-dimensional photocatalyst design: A critical review of recent experimental and computational advances, *Mater. Today*, 2020, **34**, 78–91.

26 J. Greeley, T. F. Jaramillo, J. Bonde, I. Chorkendorff and J. K. Nørskov, Computational high-throughput screening of electrocatalytic materials for hydrogen evolution, *Nat. Mater.*, 2006, **5**, 909.

27 V. Butera and M. C. Toroker, Electronic properties of pure and Fe-doped β-Ni(OH)2: New insights using density functional theory with a cluster approach, *J. Phys. Chem. C*, 2016, **120**, 12344–12350.

28 V. Butera and M. C. Toroker, Practical cluster models for a layered β-NiOOH material, *Materials*, 2017, **10**, 480.

29 V. Butera, Y. Tanabe, T. Miyazawa, T. Fujitani, M. Kayanuma and Y.-K. Choe, Mechanistic investigation on ethanol-to-butadiene conversion reaction over metal oxide clusters, *Int. J. Quantum Chem.*, 2021, **121**, e26494.

30 V. Butera, N. Fukaya, J.-C. Choi, K. Sato and Y.-K. Choe, Alkoxysilane production from silica and dimethylcarbonate catalyzed by alkali bases: A quantum chemical investigation of the reaction mechanism, *Inorg. Chim. Acta*, 2018, **482**, 70–76.

31 M. D'Arienzo, F. Gamba, F. Morazzoni, U. Cosentino, C. Greco, M. Lasagni, D. Pitea, G. Moro, C. Cepek, V. Butera, E. Sicilia, N. Russo, A. B. Munoz-Garcia and M. Pavone, Experimental and theoretical investigation on the catalytic generation of environmentally persistent free radicals from benzene, *J. Phys. Chem. C*, 2017, **121**, 9381–9393.

32 V. Butera, A. Massaro, A. B. Muñoz-García, M. Pavone and H. Detz, d-Glucose Adsorption on the TiO_2 Anatase (100) Surface: A Direct Comparison Between Cluster-Based and Periodic Approaches, *Front. Chem.*, 2021, **9**, 716329.

33 S. Kozuch and S. Shaik, How to conceptualize catalytic cycles? The energetic span model, *Acc. Chem. Res.*, 2010, **44**, 101–110.

34 S. Kozuch, A refinement of everyday thinking: the energetic span model for kinetic assessment of catalytic cycles, *Wiley Interdiscip. Rev.: Comput. Mol. Sci.*, 2012, **2**, 795–815.

35 N. Alidoust and E. A. Carter, First-principles assessment of hole transport in pure and Li-doped NiO, *Phys. Chem. Chem. Phys.*, 2015, **17**, 18098–18110.

36 A. D. Laurent, C. Adamo and D. Jacquemin, Dye chemistry with time-dependent density functional theory, *Phys. Chem. Chem. Phys.*, 2014, **16**, 14334–14356.

37 C. Adamo and D. Jacquemin, The calculations of excited-state properties with time-dependent density functional theory, *Chem. Soc. Rev.*, 2013, **42**, 845.

38 S. Wu, J. Žurauskas, M. Domański, P. S. Hitzfeld, V. Butera, D. J. Scott, J. Rehbein, A. Kumar, E. Thyrhaug, J. Hauer and J. P. Barham., Hole-mediated photoredox catalysis: Tris(p-substituted)biarylaminium radical cations as tunable, pre-complexing and potent photooxidants, *Org. Chem. Front.*, 2021, **8**, 1132–1142.

39 A. D. Becke, Density-functional thermochemistry. III. The role of exact exchange, *J. Chem. Phys.*, 1993, **98**, 5648–5652.

40 M. J. Frisch, G. W. Trucks, H. B. Schlegel, G. E. Scuseria, M. A. Robb, J. R. Cheeseman, G. Scalmani, V. Barone, G. A. Petersson, H. Nakatsuji, X. Li, M. Caricato, A. V. Marenich, J. Bloino, B. G. Janesko, R. Gomperts, B. Mennucci, H. P. Hratchian, J. V. Ortiz, A. F. Izmaylov, J. L. Sonnenberg, D. Williams-Young, F. Ding, F. Lipparini, F. Egidi, J. Goings, B. Peng, A. Petrone, T. Henderson, D. Ranasinghe, V. G. Zakrzewski, J. Gao, N. Rega, G. Zheng, W. Liang, M. Hada, M. Ehara, K. Toyota, R. Fukuda, J. Hasegawa, M. Ishida, T. Nakajima, Y. Honda, O. Kitao, H. Nakai, T. Vreven, K. Throssell, J. A. Montgomery, Jr., J. E. Peralta, F. Ogliaro, M. J. Bearpark, J. J. Heyd, E. N. Brothers, K. N. Kudin, V. N. Staroverov, T. A. Keith, R. Kobayashi, J. Normand, K. Raghavachari, A. P. Rendell, J. C. Burant, S. S. Iyengar, J. Tomasi, M. Cossi, J. M. Millam, M. Klene, C. Adamo, R. Cammi, J. W. Ochterski, R. L. Martin, K. Morokuma, O. Farkas, J. B. Foresman and D. J. Fox, *Gaussian 16, Revision C.01*, Gaussian, Inc., Wallingford, CT, 2016.

41 (*a*) T. H. Dunning, Jr. and P. J. Hay, *Modern theoretical chemistry*, ed. H. F. Schaefer, III, Plenum, New York, 1977, vol. 3, pp 1–28; (*b*) P. J. Hay and W. R. Wadt, Ab initio effective core potentials for molecular calculations – potentials for the transition-metal atoms Sc to Hg, *J. Chem. Phys.*, 1985, **82**, 270–283; (*c*) W. R. Wadt and P. J. Hay, Ab initio effective core potentials for molecular calculations. Potentials for main group elements Na to Bi, *J. Chem. Phys.*, 1985, **82**, 284–298; (*d*) P. J. Hay and W. R. Wadt, Ab initio effective core potentials for molecular calculations – Potentials for K to Au including the outermost core orbitals, *J. Chem. Phys.*, 1985, **82**, 299–310.

42 (*a*) J. P. Perdew, K. Burke and M. Ernzerhof, Generalized gradient approximation made simple, *Phys. Rev. Lett.*, 1996, **77**, 3865–3868; (*b*) J. P. Perdew, K. Burke and M. Ernzerhof, Errata: Generalized gradient approximation made simple, *Phys. Rev. Lett.*, 1997, **78**, 1396–1399; (*c*) C. Adamo and V. Barone, Toward reliable density functional methods without adjustable parameters: The PBE0 model, *J. Chem. Phys.*, 1999, **110**, 6158–6169.